Lineshapes in core-level photoemission from metals: I. Theory and computational analysis

1996 J. Phys.: Condens. Matter 8 1421

(http://iopscience.iop.org/0953-8984/8/10/014)

J. Phys.: Condens. Matter **8** (1996) 1421–1438. Printed in the UK

Lineshapes in core-level photoemission from metals: I. Theory and computational analysis

H P Hughes and J A Scarfe
Cavendish Laboratory, University of Cambridge, Cambridge CB3 0HE, UK

Received 5 October 1995, in final form 18 December 1995

Abstract. Lineshapes in x-ray core-level photoemission (XPS) reflect the local electronic environment of the atomic species from which they originate, and the excitations of the material system which reduce the emerging photoelectron's kinetic energy. For metallic systems, we show that detailed analysis of such lineshapes provides important information on the local conduction band electronic structure at distinct sites of the same atomic species. A form is derived for the core-level lineshape which is based on the spectrum of excitations in the conduction band, predominantly the formation of electron–hole pairs which screen the core-level hole produced in XPS; this is more general (but less rigorous) than the Doniach–Sunjic formulation. The lineshape is used as the basis for a numerical data analysis package—SHAPER—which extracts lineshape information from experimental XPS data by least-squares fitting. Various lineshapes derived from hypothetical conduction band profiles, and the reliability of the fitting process, are examined.

1. Introduction

Photoelectron spectroscopy is a key tool in solid state physics and chemistry, x-ray photoemission (XPS) giving information on tightly bound core electrons (and therefore on local, chemically specific effects) and ultraviolet photoemission (UPS) on delocalized band structure effects; these are often regarded as separate, if complementary, approaches to electronic structure, but the study of core-level lineshapes in XPS can also provide information on the conduction band electronic structure of metallic systems, as discussed here.

In a simple, single-particle view of XPS, the core electron, with initial binding energy E_b, is excited by a photon of energy E_{ph} to a level above the vacuum level, and leaves the solid with a measured kinetic energy given by

$$E_{KE} = E_{ph} - E_{wf} - E_b. \tag{1}$$

E_{ph} and the work function E_{wf} thus determine E_b, and the XPS spectrum consists of a series of characteristic lines superimposed on a background of inelastically scattered electrons from less tightly bound levels; the line energies identify the chemical species present (and can give their relative concentrations), but the spectrum analysis rarely proceeds further. However, the detailed lineshapes, and their dependences on more complex processes related to the electronic structure and the local atomic environment, can provide much more information, as will be shown in what follows.

Electron–electron interactions require that the $(N + 1)$-electron initial and N-electron final states of the whole system be considered explicitly; the energy balance then becomes

$$E_{KE} = E_{ph} + E_{initial\ state} - E_{final\ state} - E_{wf}. \tag{2}$$

0953-8984/96/101421+18$19.50

The apparent binding energy of the photoelectron is then $E_{initial\ state} - E_{final\ state}$, corresponding to the one-electron picture's E_b only when the transition is slow, an unrealistic assumption for XPS. The system is usually initially in its ground state, largely determining E_{KE}; but the N-electron system left behind may be in a spread of possible excited final states, producing a corresponding spread in E_{KE}. Discrete excitations of the final state produce an XPS core-level line with discrete satellite peaks to higher apparent binding energy—shake-up, or multiplet structure [1–3]; but for a continuum of final state excitations, such as within the conduction band of a metal, the line develops a tail to higher binding energy, and appears asymmetrical.

Mahan set out the theory of this photoemission lineshape (and absorption and emission spectra) for the alkali metals many years ago [4] but much current analysis of XPS core-level data is still somewhat semi-empirical [5]. The theoretical lineshape derived from Mahan's work by Doniach and Sunjic [6] (DS) apply strictly only for near-peak behaviour, but has often been used inappropriately because it provides a simple model for experimental data on metals. Following Wertheim and others [7] a more widely applicable model is developed here, accounting in greater detail for the range of possible final state excitations in the conduction band. This model is then used as the basis for an iterative fitting procedure for experimental data, implemented as a computer package—SHAPER—which is applied to the analysis from experimental data from the layered compound 2H-TaS_2 and some of its intercalates, and to 1T- and 4Hb-TaS_2, in the following papers [8].

2. Theoretical background

2.1. A model for core-level photoemission lineshapes

When a core-level photohole is suddenly created in a metal, the conduction electrons move to screen its localized potential [6, 9] creating an electron–hole pair (or pairs) with a range of energies, and reducing the kinetic energy of the photoelectron. For one excitation $(\bar{\mu}\nu)$, in which an electron is excited from state μ (of energy ε_μ) to state ν (of energy ε_ν) with probability $\Lambda^2/\varepsilon_{\mu\nu}^2$ (where $\varepsilon_{\mu\nu} = \varepsilon_\nu - \varepsilon_\mu$ and Λ is the appropriate matrix element), the probability density function (PDF) of E, the energy lost by the photoelectron, is [7, 10]

$$P_{\mu\nu}(E) = (\Lambda^2/\varepsilon_{\mu\nu}^2)\delta(E - \varepsilon_{\mu\nu}) + (1 - \Lambda^2/\varepsilon_{\mu\nu}^2)\delta(E). \tag{3}$$

For multiple excitations, the individual PDFs must be convolved, and, for small Λ^2

$$P_{tot}(E) \propto \int_{-\infty}^{\infty} \mathrm{e}^{-\mathrm{i}Et} \exp\left(\sum_{\mu\nu} \frac{\Lambda^2(\mathrm{e}^{\mathrm{i}\varepsilon_{\mu\nu}t} - 1)}{\varepsilon_{\mu\nu}^2}\right) \mathrm{d}t \tag{4}$$

is the PDF of the total loss E arising from electron–hole pair formation in the final state. The double sum over μ and ν is over all hole states below, and all electron states above, the Fermi energy (E_F); only the energy of the excitation depends on the indices μ and ν, so equation (4) can be rewritten as a single sum over all possible excitations, and since the conduction band is quasi-continuous, the sum can be replaced by an integration over all excitations of energy E':

$$P_{tot}(E) \propto \int_{-\infty}^{\infty} \mathrm{e}^{-\mathrm{i}Et} \exp\left(\int_0^{\infty} J(E') \frac{(\mathrm{e}^{\mathrm{i}E't} - 1)}{E'^2}\, \mathrm{d}E'\right) \mathrm{d}t. \tag{5}$$

(In many of the equations that follow, a function of energy is expressed as an integral of other functions of energy over a particular range of energy, and the variables E and E' are used essentially interchangeably as appropriate.) Here $J(E')$ is proportional to the density

of excitations of energy E'. Note that $P_{tot}(E)$ depends only on $J(E')$ for $E' < E$, and that the denominator E'^2 ensures that, provided $J(E')$ increases no faster than E'^2, only the low-energy part of $J(E')$ influences the lineshape.

The overall lineshape $I(E)$ can now be calculated by convolving $P_{tot}(E)$ with a delta function at $E = E_0$, the kinetic energy of core electrons emerging without energy loss, a Lorentzian lineshape to account for lifetime (λ^{-1}) broadening of the final state, and a Gaussian of width σ to include instrumental and any phonon broadening [11–13]; these are conveniently performed as multiplications in the Fourier (time) domain, giving

$$I(E) = A\int_{-\infty}^{\infty} \mathrm{e}^{-\mathrm{i}Et}\mathrm{e}^{-\mathrm{i}E_0 t}\mathrm{e}^{-\lambda|t|}\exp\left(-\frac{\sigma^2 t^2}{2}\right)\exp\left(\int_0^{\infty} J(E')\frac{(\mathrm{e}^{\mathrm{i}E't}-1)}{E'^2}\,\mathrm{d}E'\right)\mathrm{d}t \tag{6}$$

where A is a simple multiplier determining the total intensity, and is varied as a fitting parameter (see below). $J(E')$ is determined by $D(E)$, the single-electron density of states (DOS) above and below E_F (though it should also be borne in mind that the single-particle density of states may be significantly modified locally in the presence of the photoexcited core hole), and by other processes such as plasmon excitation; for the moment such other processes are ignored, and $J(E')$ is taken to be a joint density of states (JDOS):

$$J(E) = \Lambda^2\int_{E_F-E}^{E_F} D(E')D(E'+E)\,\mathrm{d}E' = \Lambda^2\int_{-\infty}^{\infty} D_{filled}(E')D_{empty}(E'+E)\,\mathrm{d}E' \tag{7}$$

where

$$D_{filled}(E') = \begin{cases} D(E') & \text{if } E' \leqslant E_F \\ 0 & \text{if } E' > E_F \end{cases} \qquad D_{empty}(E') = \begin{cases} D(E') & \text{if } E' > E_F \\ 0 & \text{if } E' \leqslant E_F. \end{cases} \tag{8}$$

Here Λ^2 is assumed the same for all excitations, effectively ignoring the symmetries of the states involved, probably an appropriate approximation when the states near E_F are of similar symmetry; if necessary, $J(E)$ could be suitably weighted by some function $\Lambda^2(E)$. So $D(E)$ and E_F determine $J(E)$ and hence the core-level lineshape $I(E)$, though detailed structure in $D(E)$ tends to become blurred by the convolutions involved. Nevertheless $D(E)$ influences the lineshape, as demonstrated below and as experimentally observed.

The DS lineshape [6] is a special case of equation (6). Assuming $D(E)$ is approximately constant near E_F for a near-free-electron metal, i.e.

$$D(E_F+\varepsilon) = D(E_F) + \varepsilon D'(E_F) + O(\varepsilon^2) + \cdots \tag{9}$$

and using equation (7), for small E'

$$J(E') = \Lambda^2 D(E_F)^2 E' = \alpha E'. \tag{10}$$

So if only excitation energies E' much less than the width of the conduction band are considered, $D(E)$ can be taken to be approximately flat and infinitely wide, and $J(E')$ taken as proportional to E'. Since the shape of $I(E)$ for small E is determined by $J(E')$ for small E', the near-peak lineshape is therefore similar for all DOSs. Using equation (10), equation (6) becomes

$$I(E) \propto \int_{-\infty}^{\infty} \mathrm{e}^{-\mathrm{i}Et}\mathrm{e}^{-\mathrm{i}E_0 t}\mathrm{e}^{-\lambda|t|}\exp\left(-\frac{\sigma^2 t^2}{2}\right)\exp\left(\alpha\int_0^{\infty}\frac{(\mathrm{e}^{\mathrm{i}E't}-1)}{E'}\,\mathrm{d}E'\right)\mathrm{d}t. \tag{11}$$

Despite the irrelevance of $J(E')$ for large E' to $I(E)$ for small E, the inner integral does not converge, so the model $J(E')$ must be refined by introducing an artificial cut-off in the JDOS at E_c, much greater than the range of E over which $I(E)$ is required:

$$J(E') = \alpha E' \text{ for } E' < E_c \qquad J(E') = 0 \text{ for } E' \geqslant E_c. \tag{12}$$

Then, for $\lambda = \sigma = 0$ (and Γ the transcendental gamma function and γ Euler's constant)

$$I(E) \propto \frac{2e^{-\alpha\gamma}\sin(\alpha\pi)\Gamma(1-\alpha)}{E_c^{\alpha}} E^{(\alpha-1)} \tag{13}$$

—the power law derived by Nozières and de Dominicis [14] as the limiting behaviour of the lineshape. α, the slope of $J(E)$ at $E = 0$, is usually called the asymmetry index. The lineshape has no characteristic width since its shape is the same on any scale. Note that equation (13) holds only for $E \ll E_c$, a very restrictive limit [6] since E_c even in alkali metals is a few electron volts. When $\lambda = 0$, convergence requires that $0 < \alpha < 1$, while for non-zero λ

$$I(E) \propto \frac{2e^{-\alpha\gamma}\Gamma(1-\alpha)}{E_c^{\alpha}} \frac{\cos(\alpha\pi/2 - (1-\alpha)\tan^{-1}(E/\lambda))}{(\lambda^2 + E^2)^{(1-\alpha)/2}} \tag{14}$$

—the widely used DS lineshape, derived by Doniach and Sunjic [6] from a different perspective. Figure 1 shows some example DS lineshapes for various values of α; as the asymmetry increases, the tail on the low-kinetic-energy side of the XPS line becomes more pronounced, and the peak height is reduced. (For simplicity, in this and all later figures, the energy scale has been left without units, but typical observed lineshapes correspond to an energy of 1 eV per unit on the scale shown. In all the lineshape figures to follow, the energy scale refers to kinetic energy relative to E_0, and the Lorentzian and Gaussian widths are $\lambda^{-1} = 0.06$ and $\sigma = 0.3$, typical of the values encountered experimentally in papers II and III [8].)

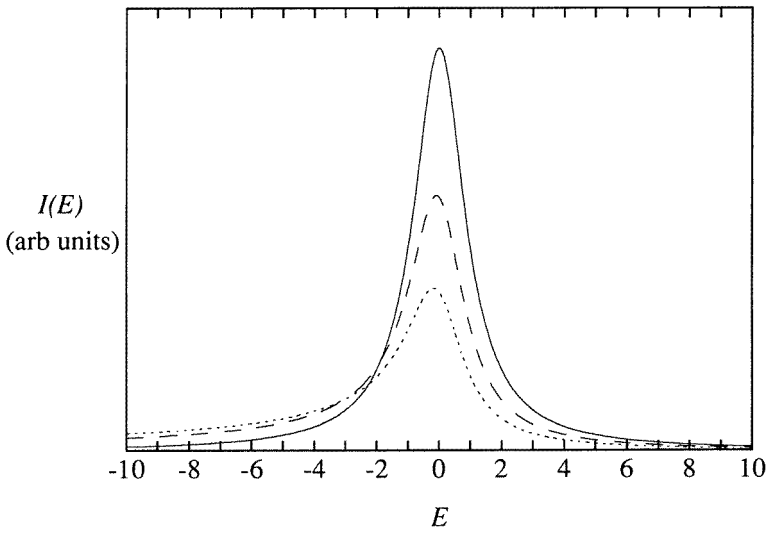

Figure 1. Some typical DS lineshapes for $\alpha = 0.0$ (——), 0.1 (- - - -) and 0.2 (·····), and with a Lorentzian width $\lambda^{-1} = 0.06$ and Gaussian instrumental width $\sigma = 0.3$. The horizontal scale refers to photoelectron kinetic energy relative to E_0, and the vertical axis is in arbitrary units.

2.2. Secondary-electron backgrounds in XPS

So far, only energy losses comprising part of the primary lineshape, intrinsic local effects, have been dealt with. But inelastic scattering of photoelectrons from shallower core levels

or bands results in a secondary-electron background on which are superposed the core lineshapes of interest, and for detailed lineshape analysis it is vital to account for this background appropriately. For a primary (unscattered) spectrum $j(E)$, the measured count rate $F(E)$ can be described by

$$F(E) = j(E) + B(E) = j(E) + \int_E^\infty K(E' - E) j(E') \, \mathrm{d}E' \tag{15}$$

where $K(\varepsilon)$ gives the probability that a photoelectron loses energy ε before detection [15–17]. Shirley [18] suggested removing $B(E)$ by taking it as proportional to the primary-photoelectron count at all higher kinetic energies, i.e. by assuming $K(\varepsilon) = K_0$ for $\varepsilon > 0$:

$$B(E) = K_0 \int_E^\infty j(E') \, \mathrm{d}E'. \tag{16}$$

K_0 is then adjusted until the background on the low-KE side of the peak matches the measured flux. $F(E)$ is used as a first approximation for $j(E)$ in equation (16) and the process iterated by calculating $B(E)$, subtracting from $F(E)$ and using the result as a better approximation for $j(E)$. Shirley's procedure, though conveniently straightforward, is unfortunately inappropriate for DS lineshapes, erroneously interpreting the asymmetric tail as part of the secondary-electron background. A more realistic loss function would involve the energy dependent dielectric function, but for metals, and for low energy losses at which plasmon excitation is irrelevant, a good approximation for $K(\varepsilon)$ is [19]

$$K(\varepsilon) = v\varepsilon \tag{17}$$

with v a constant, and this is used in all calculations here. Inelastic scattering of electrons with much higher primary energy than the line of interest are accounted for with a linear baseline, and equation (15) becomes

$$F(E) = j(E) + B(E) = j(E) + \chi - \zeta E + v \int_E^\infty (E' - E) j(E') \, \mathrm{d}E'. \tag{18}$$

This information leads to more involved calculations, but gives a more realistic background; χ, ζ and v are varied during the fitting process described in the following section.

3. Analysis of XPS data by least-squares fitting

3.1. An overview of the SHAPER package

An XPS lineshape data analysis package must derive a model lineshape using a set of relevant parameters, and iterate these (subject to suitable constraints) to minimize the difference (usually the sum of the squared residuals—the difference between the model and data at each energy) between the model and experiment. Many algorithms and library subroutines offer least-squares minimization, fitting data to any model function; but none handle the complexity of the problem addressed here, with the observed lineshape related only indirectly to the model function(s) of interest, with the computational efficiency required. So a photoemission data-analysis package, SHAPER, has been developed for analysing XPS data with resolution and signal-to-noise ratio sufficiently good to differentiate between lineshapes derived from different conduction band structures; it allows fitting to a range of possible DOS and JDOS functions, offering a more comprehensive approach than hitherto available.

SHAPER involves the iterative minimization of a 'goodness-of-fit parameter' defined as

$$\rho(\xi_1, \xi_2, \xi_3, \ldots, \xi_\mu) = \sum_{i=1}^{n} \frac{(d_i - \theta(E_i, \xi_1, \xi_2, \xi_3, \ldots, \xi_\mu))^2}{\eta_i^2} \tag{19}$$

where d_i is the number of photoelectrons counted at energy E_i and n is the number of experimental points. η_i is an estimate of the standard deviation of d_i, and μ is the number of parameters, ξ_j, of the model lineshape which has the value $\theta(E_i, \xi_1, \xi_2, \xi_3, \ldots, \xi_\mu)$ at energy E_i. ρ is iteratively minimized with respect to parameters ξ_j, to obtain the most probable set, but because there may be local minima for ρ, the fitting process must begin in a region of the μ-dimensional parameter space sufficiently close to the absolute minimum of ρ; i.e., the parameters must initially be adjusted manually to fairly close to those of the best-fit model. The parameters ξ_j are those determining lineshape itself (λ and σ, and the β parameters; see below), A determining its overall strength, E_0 determining its position, and χ, ζ and v determining the background. To avoid wild excursions in the minimization process, limiting bounds can also be imposed on the variation of particular parameters. In cases in which several lines are simultaneously fitted, as for multiplet structures such as those addressed in papers II and III, corresponding parameters for different components of the multiplet can also be constrained to be equal.

3.2. A numerical implementation of the lineshape model

SHAPER requires a method reliably and quickly calculating $I(E)$ from $J(E)$ and other parameters using a numerical implementation of equation (6). $J(E)$ is the key to the lineshape, but closed form solutions for $I(E)$ are possible only for very simple forms of $J(E)$, and then only for small E. Fortunately equation (6) is readily amenable to numerical methods, particularly fast Fourier transforms (FFTs), and SHAPER finds $I(E)$ when $J(E)$ is

(i) specified algebraically;

(ii) obtained by convolution from an algebraic model $D(E)$, together with a value for E_F.

Table 1 gives the functional forms for $J(E)$ programmed as options in SHAPER. (These were all designed to fit real data, so are often more complicated than required to produce the sample lineshapes of subsection 3.3 below; the numbering scheme and the ordering of parameters β_j reflect this.) There are two conditions on $J(E)$: (i) $J(0) = 0$ (see equation (7); optd = 4 violates this, but $J(0) \ll 1$ if $\beta_1 \gg \beta_2$); (ii) $J(E) \to 0$ as $E \to \infty$ so that the integrals in equation (6) converge. Both apply for all the values of the parameters β_j permitted in the fitting process. β_1–β_5 are named according to their effects on $J(E)$; e.g., for optd = 7, β_1 is the 'cut-off position' and β_2 the 'cut-off sharpness'. Other names can be obviously identified with their corresponding parameters, and are used in SHAPER's output. As examples, figure 2 shows $J(E)$ for two different models specified in the caption; the peak was introduced for optd = 8 to represent extrinsic plasmon losses in the lineshape of 2H-TaS_2—see paper II [8]—and then $J(E)$ should properly be referred to as the joint density of excitations rather than the JDOS.

Table 2 gives the functional forms for $D(E)$ programmed in SHAPER, and one of these is plotted in figure 3(a) for optd = 3 and some typical parameter values for two values of E_F. When $J(E)$ is determined from $D(E)$, there is a complication because $D(E_F)$ depends on the parameters, β_j, that specify $D(E)$; the slope of $J(E)$ at $E = 0$ is not independent of

Table 1. The functional forms used for $J(E)$ in SHAPER. α is dimensionless, and the other parameters have dimensions of energy except for the sharpness parameter β_2 which has dimensions of inverse energy.

Functional form of $J(E)$	Description	optd
$\alpha E \exp(-E/\beta_1)$	A straight line at the origin which falls away slowly, reaching its maximum at β_1 (implemented as a special case of optd = 4)	↓
$\alpha E \exp(-E/\beta_4) + \alpha\beta_3 \exp(-(E-\beta_1)^2/2\beta_2^2)$	As above but with a Gaussian peak added at position β_1 with width parameter β_2 and height β_3	4
$\alpha E \exp(-E/\beta_4) + \alpha E\beta_3 \exp(-(E-\beta_1)^2/2\beta_2^2)$	As optd = 4 but with E multiplying the Gaussian to force it to zero at $E = 0$	6
$\frac{\alpha E}{2}(1 - \tanh(\beta_2(E-\beta_1)))$	A straight line until reaching a smooth cut-off at β_1, sharpness β_2	7
$\frac{\alpha E}{2}(1 - \tanh(\beta_2(E-\beta_1))) + \beta_5\alpha E \exp(-(E-\beta_3)^2/2\beta_4^2)$	As optd = 7 but with a Gaussian peak added	8

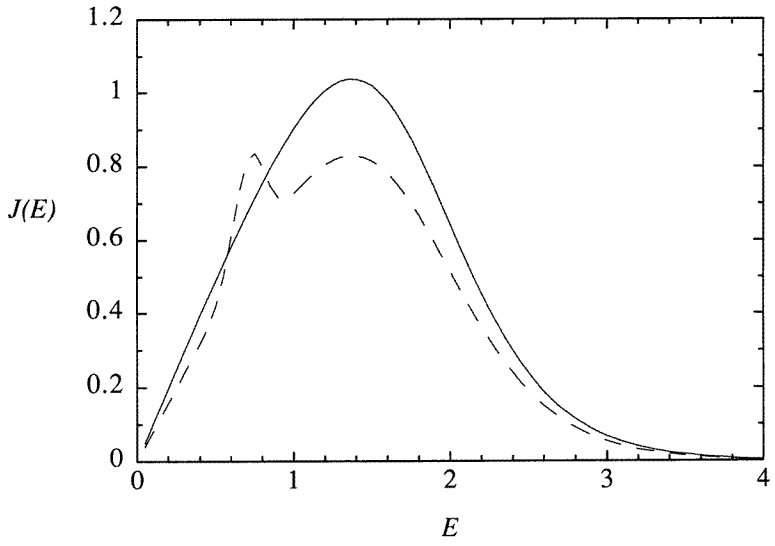

Figure 2. Some examples of the model JDOS functions $J(E)$ used in SHAPER with parameters as follows:

	optd	α	β_1	β_2	β_3	β_4	β_5
——	8	1.0	1.75	1.5	—	—	0
- - - -	8	0.8	1.75	1.5	0.7	0.1	1

these parameters and thus α cannot itself be specified as is the case when $J(E)$ is specified directly (equation (10)). Instead, α is retained as a scaling factor for $J(E)$ in cases when $D(E)$ is used for fitting, and the value obtained cannot be directly compared with α from fitting using a specific $J(E)$. For the examples in figure 3, $D(E_F) \approx 1$, so with $\alpha = 1$, the

Table 2. The functional forms used for $D(E)$ in SHAPER.

Functional form of $D(E)$	Description	optd
$\exp(-E^2 \ln 2/\beta_1^2)$	A single Gaussian peak of half width β_1 at half maximum, with $E_F = \beta_2$	1
$\exp(-E^2 \ln 2/\beta_1^2) + \beta_3 \exp(-(E-\beta_4)^2 4 \ln 2/\beta_2^2)$	A pair of Gaussians of half widths β_1 and β_2, height ratio β_3, separation β_4	2
$\dfrac{\tanh(\beta_1 E) - \tanh(\beta_1(E-\beta_2))}{2}$	A 'top hat' function with sides of steepness β_1 and with overall width β_2	3

initial slope of $J'(0)$ is ≈ 1 close to α; but when $D(E_F) \not\approx 1$ this is no longer the case, and the derived $J(E)$ must be inspected to obtain the asymmetry parameter from the initial slope.

Even relatively simple model DOSs, like those in figure 3(*a*), give algebraically complicated JDOSs after applying equation (7), and new models can be introduced only at considerable cost in programming and execution times. The models have therefore been kept as flexible as possible, and an explicit $J(E)$ has been used where this can be done with acceptable realism; the advantages of doing so will be explored in subsection 3.4.

3.3. Some example lineshapes from the SHAPER package

Lineshapes derived from some of the models are illustrated in figures 4–8; each figure shows the theoretical lineshape $I(E)$ expected for the JDOS in the inset panel. In each case the vertical scale for $I(E)$ is arbitrary, and no background has been included.

Figure 4 shows the lineshape for various values of $\alpha(= J'(0))$ for a linear JDOS that cuts off exponentially to zero at $E = +3$. It is identical to the DS lineshape for as far in energy below zero as the JDOS remains linear, and, as for the simplistic DS JDOS, the peak height is strongly dependent on α. The asymmetric tail has a shoulder, corresponding to the JDOS cut-off, at $E = -3$; this is less marked for lower values of α and could easily be lost in any inelastic background (not included here) and only be apparent when the lineshape is fitted computationally. Just perceptible is the movement of the peak maximum to lower KE as α increases. Figure 5 varies the cut-off energy, and the shoulder shifts accordingly; note that even though $J(E)$ for the two highest cut-off positions is identical up to $E = 5$, the extra transitions available at higher energy shift weight to lower KE and cause the observed peak heights to differ.

Figure 6 superposes a Gaussian peak of specified height, width and position (β_3) on $J(E)$ (optd = 8); such a JDOS is unlikely to result from a real DOS, but this form is essential to include extrinsic excitations other than electron–hole pairs, such as plasmon losses. The example is exaggerated to demonstrate how pronounced the peak in $J(E)$ must be to give a satellite in the photoemission lineshape. The line for $\beta_3 = 1$ also shows a weak feature at $E = -2$ corresponding to a double excitation; such multiple excitations are automatically incorporated by SHAPER, but are very weak effects.

When SHAPER generates $J(E)$ algebraically as a convolution of $D(E)$ (for a particular E_F), the slope of $J(E)$ at $E = 0$ is not determined by a single parameter (α) as is the case when $J(E)$ is itself specified, but is derived from those which determine $D(E)$; $D(E)$ and $J(E)$ must therefore be examined graphically for comparison with other results obtained using algebraically specified $J(E)$s as discussed above. It is also not possible to invert the convolution to derive $D(E)$ from $J(E)$, as many different models for the DOS could

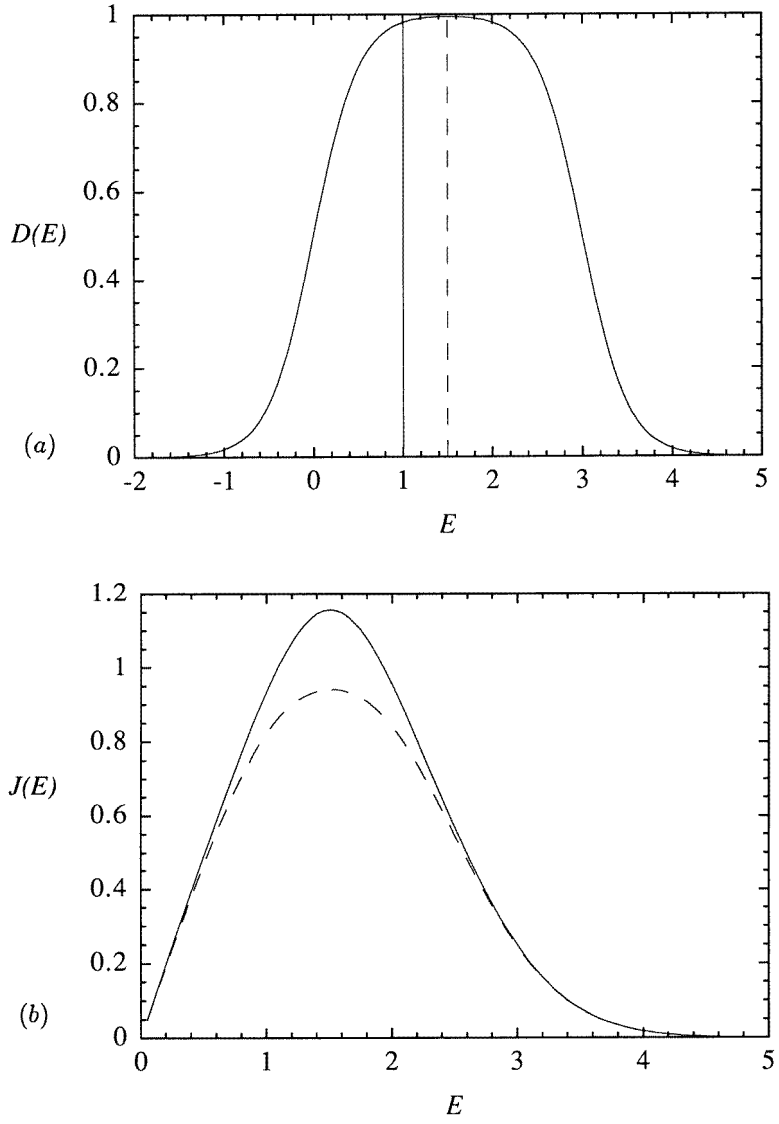

Figure 3. (*a*) An example of the model DOS functions $D(E)$ used by SHAPER, with optd = 3, $\beta_1 = 2$ and $\beta_2 = 3$. —— and - - - - represent $E_F = 1$ and 1.5 respectively. (*b*) The corresponding functions $J(E)$.

produce closely similar JDOSs. Figure 7 uses a $J(E)$ calculated from a DOS $D(E)$ which has Gaussian form centred on $E = 0$ (optd = 1), with HWHM $\beta_1 = 6$ and E_F (i.e. β_2) $= 0$. The corresponding $J(E)$ is linear at $E = 0$ and smoothly falls away, so the lineshape is of the DS form close to the peak, falling away to zero at an energy of the order of the width of the DOS and with no sharp features. The curves show the effect on the lineshape of varying the height of the Gaussian such that the resulting initial slope of $J(E)$ (i.e. α) varies. Figure 8 shifts E_F (a parameter that, as will be seen in paper II, is experimentally adjustable in intercalated materials), changing the occupation of the conduction band while

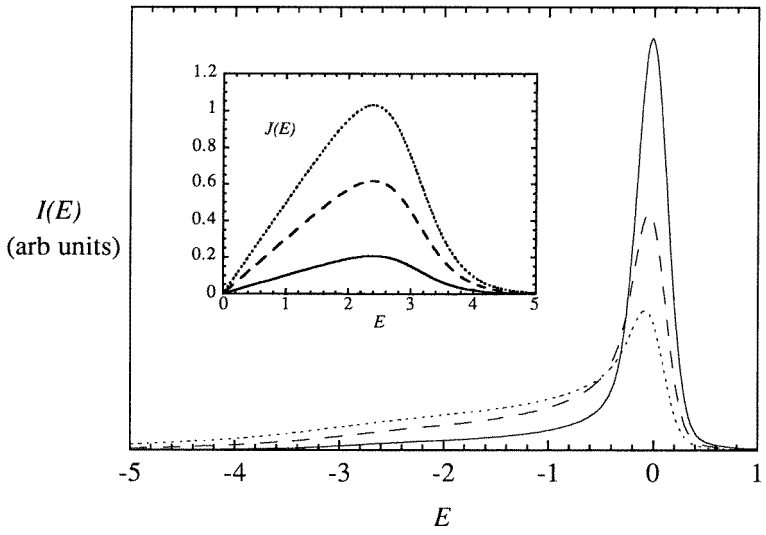

Figure 4. The effect on the lineshape, generated using optd = 7, of changing the asymmetry parameter α, determined by the slope of the JDOS $J(E)$ at the origin (see the inset). E is the kinetic energy shift from the 'true' line energy E_0, and for these curves the cut-off energy $\beta_1 = 3$, the cut-off sharpness $\beta_2 = 1.5$, and α is 0.1 (——), 0.3 (- - - -) or 0.5 (· · · · · ·).

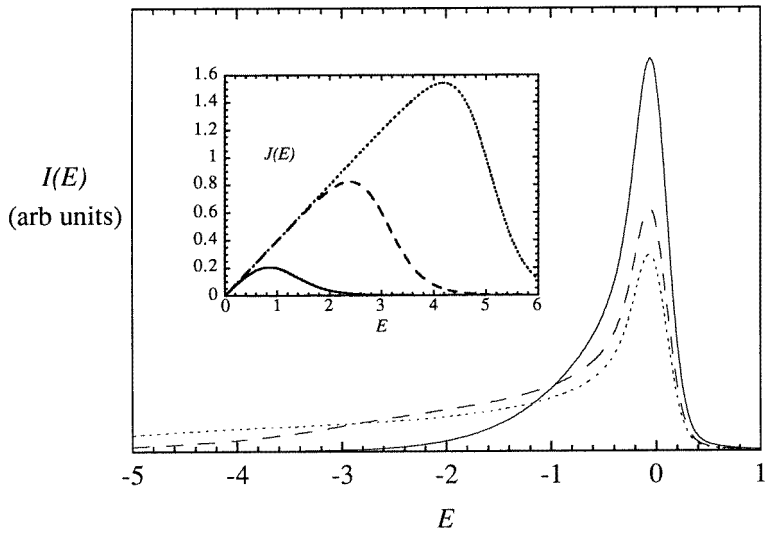

Figure 5. The effect on the lineshape, generated using optd = 7, of changing the energy of the cut-off in the JDOS (shown in the inset). Here $\alpha = 0.40$ and the cut-off sharpness $\beta_2 = 1.50$ for all the curves, and the cut-off energies are $\beta_1 = 1.00$ (——), 3.0 (- - - -) and 5.0 (· · · · · ·).

the DOS remains fixed; note how the lineshape changes markedly even for small shifts in E_F.

These calculated lineshapes show several clear trends: (i) increasing the slope of $J(E)$ at $E = 0$ increases the asymmetry close to the peak; (ii) sharp features in $J(E)$ appear in the

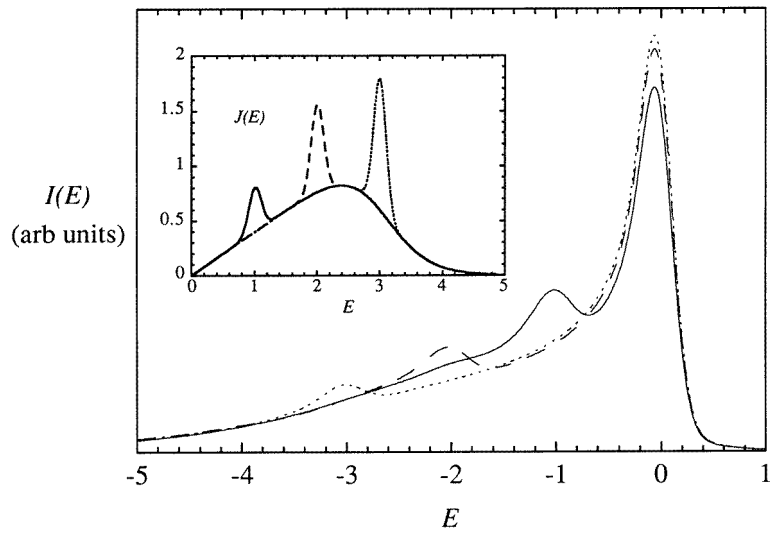

Figure 6. The effect on the lineshape of introducing an additional peak structure in the effective JDOS as for optd = 8. Here $\alpha = 0.40$, the cut-off sharpness $\beta_2 = 1.50$, the cut-off energy $\beta_1 = 3.0$, the peak width $\beta_4 = 0.1$ and the peak-to-slope ratio $\beta_5 = 2.0$ for all the curves; the peak positions are $\beta_3 = 1.00$ (——), 2.0 (- - - -) and 3.0 (· · · · · ·).

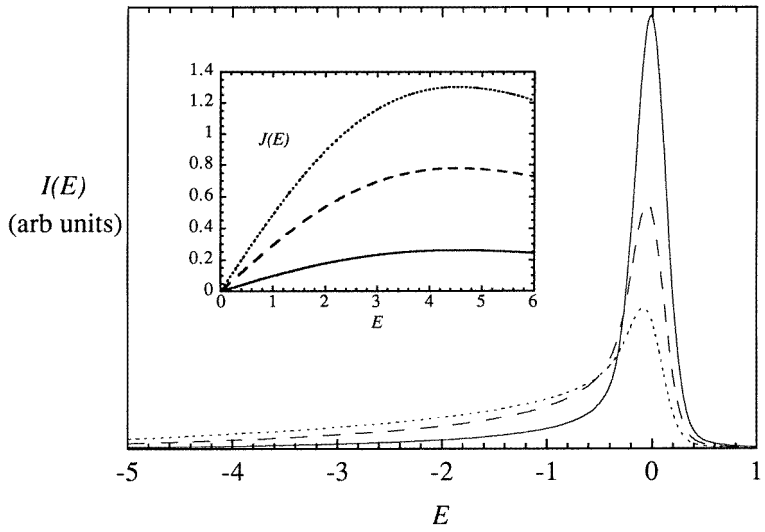

Figure 7. Here $J(E)$ is calculated from a DOS $D(E)$ which has Gaussian form centred on $E = 0$ (optd = 1), with HWHM $\beta_1 = 6$ and E_F (i.e. β_2) = 0. The curves show the effect of varying the height of the Gaussian such that $J'(0)$ (i.e. α) varies: $\alpha = 0.1$ (——), 0.3 (- - - -) and 0.5 (· · · · · ·).

lineshape, $I(E)$, but considerably smoothed—peaks in $J(E)$, unless very narrow, appear as shoulders in the lineshape; (iii) the $J(E)$ functions (and the corresponding lineshapes) calculated from explicit $D(E)$ functions are generally very similar to those which can be

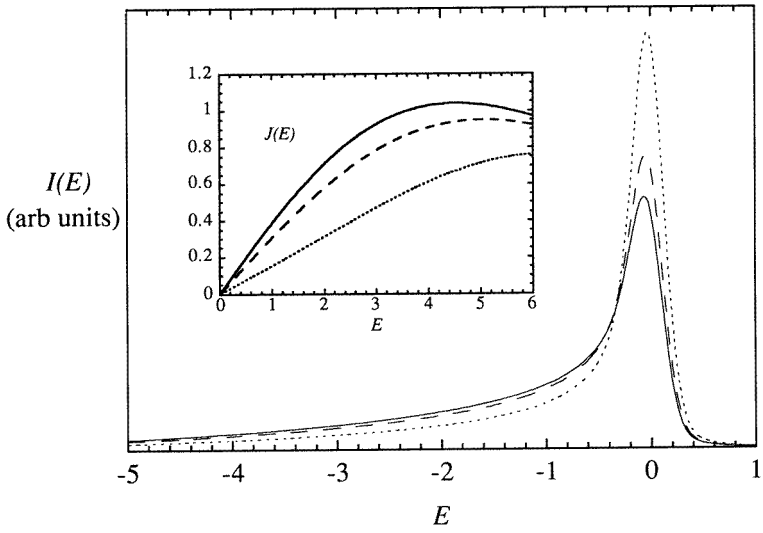

Figure 8. As for figure 7, but here E_F is varied while α is fixed at 0.40 by fixing the Gaussian peak height. $E_F = 0.0$ (——), 1.0 (- - - -) and 2.0 (· · · · · ·). As E_F increases, the DOS at E_F falls because of the Gaussian profile of the DOS, and so therefore do the initial slope of $J(E)$ and the effective asymmetry.

specified directly in SHAPER. A comparison of the $J(E)$ models generated in figures 7 and 8 with the explicit, arbitrary $J(E)$ models of figure 4–6 reveals that the explicit models do indeed successfully simulate the $J(E)$ derived from a variety of different $D(E)$ functions. Figures 7 and 8 should therefore not be viewed as a wholly distinct method of calculating the lineshapes, but rather as an extension of the previous set, demonstrating how the changes in $J(E)$ might be related to changes in $D(E)$.

3.4. Some example fits from the SHAPER package

SHAPER's reliability was tested using data artificially generated with specified lineshape parameters with random noise added. SHAPER's output parameters should of course be the same, with appropriate error bounds, as those used to generate the data, and not be overly sensitive to the initial estimate of parameters. The error bounds should also correspond to those observed by 'Monte Carlo simulations' [20], which indicate how accurately the final parameter set has been determined. Further, when attempting to fit data generated from one algebraic form of $J(E)$ with a model lineshape derived from a different $J(E)$, the model should be rejected as unsuitable unless the $J(E)$ returned by the fit is, over a wide range of E, almost identical to that used for generating the lineshape.

First, two lineshapes (lines A and B, shown in figure 9) were generated using respectively optd = 7 (table 1) as in figures 4 and 5, and optd = 1 (table 2) as in figures 7 and 8. A and B were then used to produce 20 'real' spectra (datasets A and B) by adding random numbers with a Gaussian distribution (mean, zero; standard deviation, $\sqrt{100 + N}$, where N is the number of counts at the relevant energy in the original lineshape) to simulate noise. Constant backgrounds were included to allow noisy 'data' to dip below the base line of the peak without becoming negative. Dataset A′ was generated from lineshape A with 'worse' noise of standard deviation $\sqrt{900 + N}$. These datasets were then fitted with a

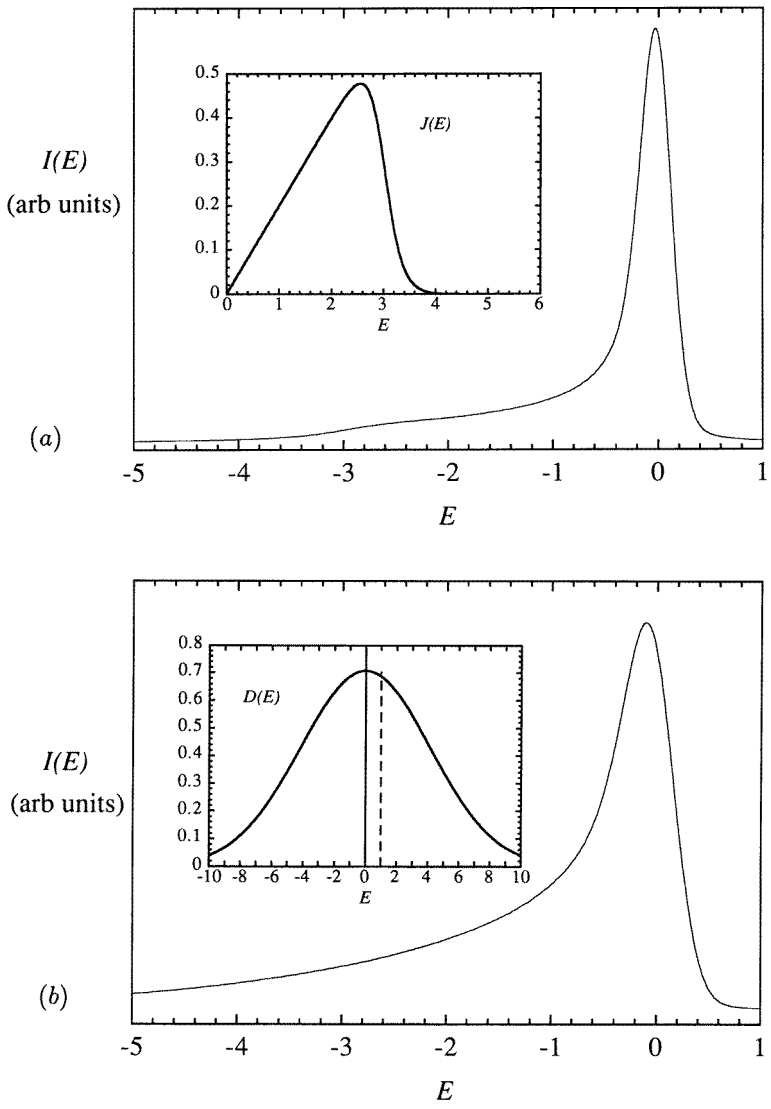

Figure 9. The original lineshapes from which the test data were derived. (*a*) Line A is based on a linear $J(E)$ with a cut-off at $E = -3.0$, a cut-off sharpness of 3.0, and with $\alpha = 0.20$. (*b*) Line B is based on a Gaussian $D(E)$ with half width 5.0 and E_F offset by 1 energy unit from the peak maximum (- - - -); this produces a $J(E)$ with an initial slope (i.e. α) of 0.5.

variety of lineshapes based on several different models for $J(E)$ and $D(E)$, some of them using different algebraic forms from those used for the original lines, producing in each case 20 results for the various fitting parameters involved; these 20 results thus provided estimates of the standard deviations of the fitting parameters as well as their means, and thus a measure of the reliability of the fitting process.

An example of fitting a line from dataset A using a $J(E)$ with the same mathematical form as used to generate line A, i.e. optd = 7, is shown in table 3, which lists the original values used to generate line A, the starting estimates and bounds for the fitting parameters

and the final values produced from SHAPER. The initial estimates of the parameters are very different from the original values, but the fitted parameters are very close to the original set. The reliability of such a fit is characterized by examining the results for fits to all 20 lines of dataset A which are summarized in table 4, which shows the means and standard deviations of the 20 ρ-values obtained, and of the 20 results returned for α, β_1 and β_2, together with the original parameters. The quality of fit is also represented graphically in figure 10 by comparing the original $J(E)$ with an average of the 20 $J(E)$s returned from the output parameters from SHAPER. The dashed lines indicate $\pm$one standard deviation (obtained from the 20 values of $J(E)$ at any particular point), and the dotted lines the most extreme $J(E)$ obtained. α (the slope of $J(E)$ at the origin) and the cut-off energy are determined very precisely, though the sharpness of the cut-off is less precisely retrieved because $J(E)$ is less sensitive to this parameter. The mean fitted $J(E)$ coincides with the original.

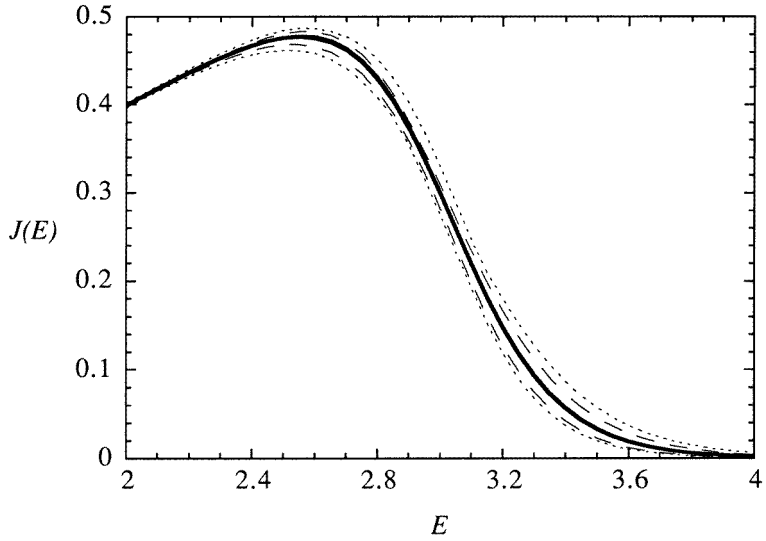

Figure 10. Results of fits of dataset A with a model $J(E)$ of the same form as used to generate line A (optd = 7). The original (——) and the mean of the fitted (——) $J(E)$s coincide almost exactly and can barely be distinguished in the figure; the spread in the fitted $J(E)$s is represented by the dashed lines (- - - -), and the extreme curves by the dotted lines (· · · · · ·).

The anticipated distribution (χ^2_ν) of ρ is characterized by $\nu = N - \mu$ (where μ is the number of free parameters in the fit (= 8 for optd = 7) and N (= 500) is the number of data points) and is approximately normal for large ν, with mean ν and variance 2ν, suggesting an expectation value of $492 \pm 31/\sqrt{20}$ for ρ for each fit; the fit corresponding to figure 10 gives $489.7 \pm 28.8/\sqrt{20}$, well within the expected range. ρ is very sensitive to the weighing factors η_i^2, being inversely proportional to any overall error, so if η_i^2 were consistently overestimated by 5%, the expectation value of ρ would be reduced by 5%, from about 490 to about 470. The reliability with which ρ can be used as a goodness-of-fit parameter thus depends on accurate estimates of the noise level. Because the artificially generated data have a specified noise level, ρ adheres closely to the expected χ^2_ν distribution, but such precision cannot be expected when dealing with experimental data where the noise level is not so well determined. Several different initial estimates of the parameters were also made; the results are not shown here, but SHAPER returned essentially the same

Table 3. The parameters used to generate the artificial data, line A, using optd = 7 (first column), and the values returned by SHAPER after fitting the artificial data with a lineshape of the same form as optd = 7 (final column). The middle three columns show the values input to SHAPER as starting points for the fitting process, and the upper and lower bounds constraining the process against wild excursions. Several decimal places are shown for the final values to emphasize that, though very close, they are not exactly the same as the originals.

	Original value	Lower bound	Upper bound	Starting value	Final value
Background level	100	0	8000	1000	101.0
Amplitude (a simple scaling factor)	300	0	12 000	300	297.8
Position (E_0)	0.00	−1.000	1.000	0.100	−0.001
Lorentzian width (λ^{-1})	0.06	0.01	0.12	0.02	0.054
Gaussian width (σ)	0.30	0.10	0.60	0.50	0.307
α	0.20	0.05	0.60	0.30	0.199
Cut-off position (β_1)	3.00	1.0	6.0	2.0	2.976
Cut-off sharpness (β_2)	3.00	0.5	5.0	1.0	3.027

Table 4. A summary of the original values for various relevant lineshape parameters used to generate lines A and B, and the mean values and standard deviations returned by SHAPER from fitting the corresponding 20 noisy datasets; also shown are the goodness-of-fit parameters ρ for each fitting process. The fits are represented graphically in figures 10–12. The figures in brackets are the values returned from fitting the noisier dataset A′ based on line A.

	Parameter	Original value	Mean fitted value	Standard deviation
Figure 10	ρ	—	489.7	28.8
Dataset A (A′)	optd	7	7	—
	α	0.200	0.200 (0.201)	0.001 (0.003)
	Cut-off (β_1)	3.000	2.995 (3.001)	0.015 (0.035)
	Cut-off (β_2) sharpness	3.000	2.979 (3.072)	0.292 (0.547)
Figure 11	ρ	—	2168.2	96.3
Dataset A	optd	7	6	—
	α	0.200	0.263	0.002
Figure 12	ρ	—	495.4	40.1
Dataset B	optd	1	1	—
	α	0.500	0.531	0.114
	Peak half width (β_1)	5.000	4.937	0.253
	E_F(β_2)	1.000	0.857	0.573

parameter set in each case.

Table 4 also summarizes the results of fitting dataset A′ with optd = 7, and it can be seen that α, β_1 and β_2 are recovered satisfactorily, though, as would be expected, with somewhat larger standard deviations; this is particularly noticeable for β_2, to which the lineshape is least sensitive. The graphical representation corresponding to figure 10 is not shown, but has exactly the same form but with somewhat larger spreads as would be expected. The results of fitting dataset A using $J(E) = E\mathrm{e}^{-E/\beta_4}$ (optd = 6 with $\beta_3 = 0$) as a model fit are shown in table 4 and figure 11, demonstrating the poor fit when the model $J(E)$ cannot reproduce the original JDOS. Despite the high values of ρ, the results are quite self-consistent, all the $J(E)$ curves lying in a narrow band and the fitted parameters having

low variances; note also that the fitted $J(E)$ is quite close to the original near $E = 0$, which dominates the lineshape, but such a fit, with $\rho = 2168$ (more than four times the expected value), would properly be rejected.

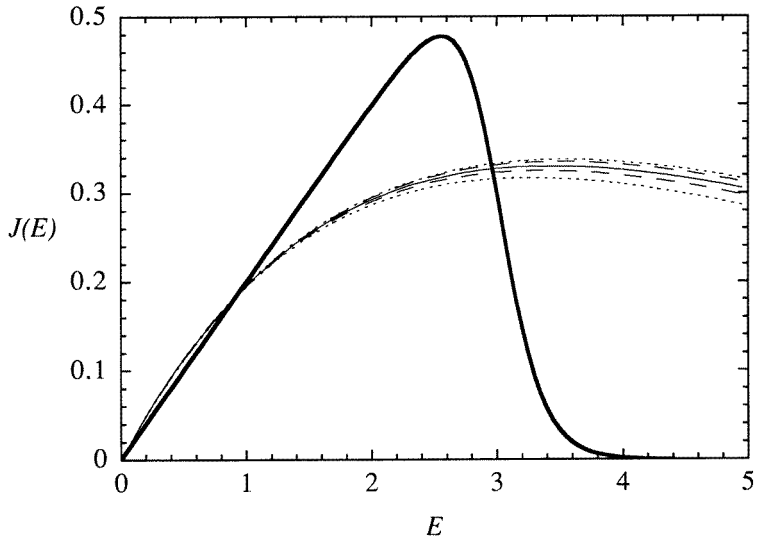

Figure 11. Results of fits of dataset A with an inappropriate model $J(E)$ ($\sim E\exp(-E)$) of different form from that used to generate line A (optd = 7). The original $J(E)$ (——) is not well fitted by the $J(E)$ (——) derived from SHAPER.

Table 4 and figure 12 similarly summarize the results of fitting dataset B using the same model for fitting as for generating the data (optd = 1, a Gaussian $D(E)$, with E_F displaced from the centre of the peak), with all the parameters free to vary. The mean and standard deviation of ρ are as expected, but, while the peak width is consistently close to the original, E_F and α are wildly scattered and raise doubts about the overall validity of the fits. Figure 12 confirms this, showing that whereas the mean $J(E)$ matches the original very closely (hence the expected ρ-values), the fitted $D(E)$ fluctuates widely. The problem here is one of uniqueness—an increase in the overall height of the DOS, accompanied by an appropriate shift of E_F away from the peak, can leave $D(E_F)$ unchanged with little effect at the lower end of $J(E)$ where the fitting is most effective; if different $D(E)$ functions produce the same (or very similar) $J(E)$ functions, SHAPER cannot readily distinguish them. So obtaining ρ-values close to those statistically expected is not in itself confirmation that a good, physically reasonable fit has been achieved when the fitting is carried out using convolution of $D(E)$ rather than a directly modelled $J(E)$. Overall, whereas dataset A is fitted well by the model JDOS used to generate it and not by others, dataset B is much less sensitive to the model DOS; it can also be concluded that the sharper features of the JDOS are more reliably predicted with SHAPER, as might be expected.

4. Conclusion

Given the 'correct' model for $J(E)$ SHAPER is capable of returning a best-fit set of parameters that is accurate and reliable, and independent of the starting parameter estimates. With the 'wrong' model for $J(E)$, SHAPER returns high (poor) values for ρ; however, since

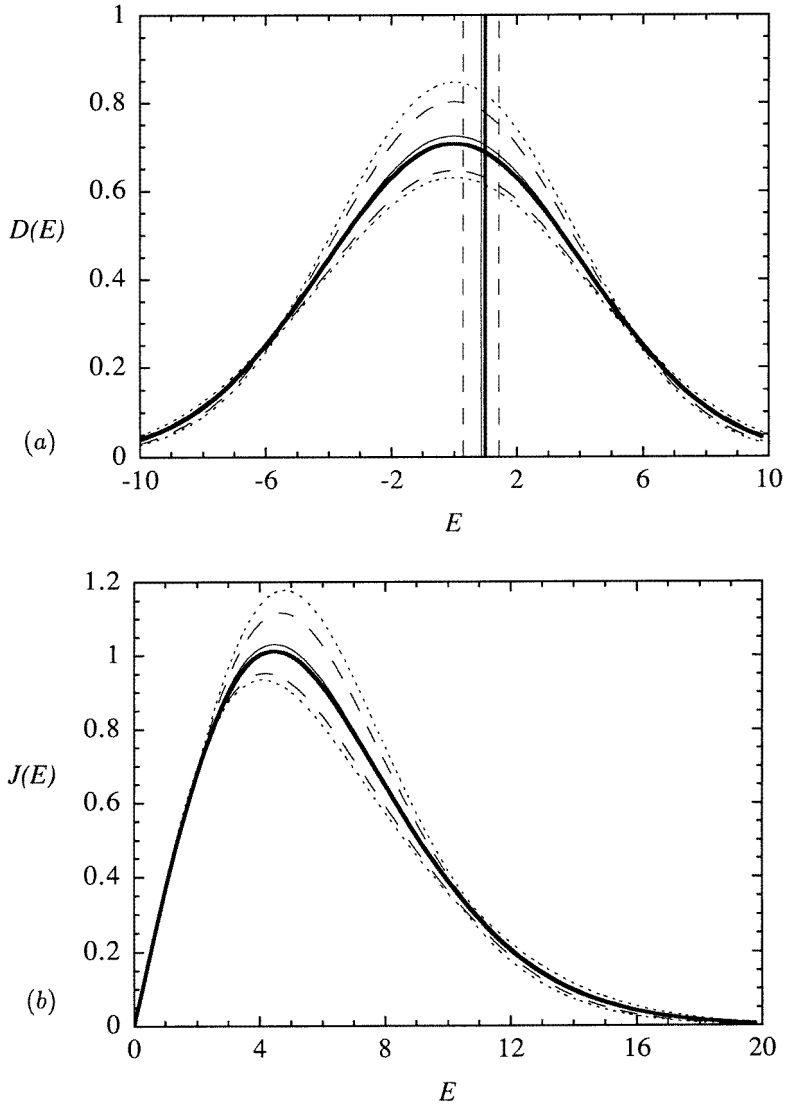

Figure 12. Results of fits to dataset B using optd = 1, the same Gaussian $D(E)$ as used to generate the noisy data. The original (——) and mean (——) of the fitted forms of $D(E)$ are in fair but not close agreement over the range plotted, with spreads in the fitted results represented by the dashed and dotted lines as for figures 10 and 11 (*a*). The vertical lines represent the original value of E_F (——), and the mean (——) and standard deviations (- - - -) of the fitted values. The fitted $J(E)$s (——) however agree quite accurately with the $J(E)$ (——) derived from the original $D(E)$ (*b*).

the lineshape depends on the values of $J(E)$ rather than its algebraic form, the shape of $J(E)$ returned must be examined, rather than just the output parameters, since different algebraic representations of the JDOS can, with suitable parameter values, give the same shape to $J(E)$. The determination of $D(E)$ is much less reliable than that of $J(E)$ because a range of $D(E)$ models can give very similar $J(E)$ functions; the generation of the lineshape

from $D(E)$ is helpful only when most of the parameters are fixed, for example when the shape of $D(E)$ is known and E_F is required. With these limitations clearly in mind, and the fact that the process must be interactive, SHAPER can be applied to data obtained from real, and complicated, physical systems [8].

Acknowledgments

This work was supported by the UK Engineering and Physical Science Research Council. The authors also gratefully acknowledge conversations with Dr M C Payne.

References

[1] Cox P A and Orchard F A 1970 *Chem. Phys. Lett.* **7** 273
[2] Cohen R L, Wertheim G K, Rosencwaig A and Guggenheim H J 1972 *Phys. Rev.* B **5** 1037
[3] Fadley C S 1978 *Electron Spectroscopy, Theory, Techniques and Applications* (London: Academic) p 1
[4] Mahan G D 1967 *Phys. Rev.* **163** 612
[5] Desimoni E, Casella G I, Cataldi T R I and Malitesta C 1989 *J. Electron Spectrosc. Relat. Phenom.* **49** 246
[6] Doniach S and Sunjic M 1970 *J. Phys. C: Solid State Phys.* **3** 285
[7] Wertheim G K and Citrin P H 1978 *Photoemission in Solids* vol 1 (Berlin: Springer) ch 5, p 201
[8] Hughes H P and Scarfe J A 1996 *J. Phys.: Condens. Matter* **8** 1439–55, 1457–73; 1995 *Phys. Rev. Lett.* **74** 3069
[9] Hopfield J J 1969 *Comment. Solid State Phys.* **2** 40
[10] Scarfe J A 1994 *PhD Thesis* University of Cambridge
[11] Citrin P H, Eisenberger P, Marra W C, Aberg T, Utriainen J and Källne E 1974 *Phys. Rev.* B **10** 1762
[12] Citrin P H, Eisenberger P and Haman D R 1974 *Phys. Rev. Lett.* **33** 965
[13] Matthew J A D and Devey M G 1974 *J. Phys. C: Solid State Phys.* **7** L335
[14] Nozières P and de Dominicis C T 1969 *Phys. Rev.* **178** 1097
[15] Tougaard S and Sigmund P 1982 *Phys. Rev.* B **25** 4452
[16] Tougaard S and Jørgensen B 1984 *Surf. Sci.* **143** 482
[17] Tougaard S 1984 *Surf. Sci.* **139** 208
[18] Shirley D A 1972 *Phys. Rev.* B **5** 4709
[19] Jouaiti A, Mosser A, Romeo M and Shindo S 1992 *J. Electron Spectrosc. Relat. Phenom.* **59** 327
[20] Press W H, Teukolsky S A, Vetterling W T and Flannery B P 1992 *Numerical Recipes* (Cambridge: Cambridge University Press) ch 15, p 691